Application of X-Ray Pulsar Navigation: A Characterization of the Earth Orbit Trade Space

Wayne H. Yu, Navigation and Mission Design Branch,
NASA Goddard Space Flight Center

Biography

Mr. Wayne Yu is a flight dynamics engineer at the NASA Goddard Spaceflight Center in the navigation and mission design branch. He is involved in various flight projects in both trajectory design and navigation. Projects include libration point trajectory design for the James Webb Space Telescope and the ARTEMIS mission, formation flight design with the Magnetospheric MultiScale Mission, and stochastic estimation and navigation design with the SEXTANT mission. He received his B.S. in 2010 and then his M.S. in 2015 in Aerospace Engineering at the University of Maryland, College Park.

Abstract

X-ray pulsar navigation (XNAV) is a celestial navigation system that uses the consistent timing nature of X-ray photons from milli-second pulsars (MSP) to perform space navigation. The challenge of XNAV comes from the faint signal, availability, and distant nature of pulsars. This paper is a study of extended Kalman filter (EKF) tracking performance within a wide trade space of bounded Earth orbits using only XNAV measurements. The study uses a simulation of existing X-ray detector space hardware. An example of an X-ray detector for XNAV is the NASA Station Explorer for X-ray Timing and Navigation (SEXTANT) mission, a technology demonstration of XNAV set to perform on the International Space Station (ISS) in 2017.

This study in particular defines the Earth orbits as Keplernian elements and varies each element individually to observe XNAV performance. It shows that the closed Earth orbit for XNAV performance relies on the orbit semi-major axis and eccentricity as well as orbit inclination. These parameters drive pulsar measurement availability and quality by influencing the natural spacecraft orbit dynamics. The orbit angles of argument of perigee and right ascension of the ascending node help define the orbit and its initial XNAV measurements. Sensitivity to initial orbit determination error growth due to the scarcity of XNAV measurements within an orbital period require appropriate timing of initial XNAV measurements.

List of Abbreviations

AOP	Argument of Periapsis
CRLB	Cramér-Rao Lower Bound
ECI	Earth Centered Inertial
ECC	Eccentricity
EKF	Extended Kalman Filter
GEO	Geosynchronous Earth Orbit
GMAT	General Mission Analysis Tool
INC	Inclination
ISS	International Space Station
LEO	Low Earth Orbit
MSP	Millisecond Pulsar
NASA	National Aeronautics and Space Administration
NICER	Neutron-star Interior Composition ExploreR
NOAA	National Oceanic and Atmospheric Administration
RAAN	Right Ascension of Ascending Node
RIC	Radial, In-track, Cross-track Spacecraft-fixed Rotating Reference Frame
RSS	Root Sum Square
SAA	South Atlantic Anomaly
SEXTANT	Station Explorer for X-ray Timing and Navigation Technology
SMA	Semi-Major Axis
STMD	Space Technology Mission Directorate
TA	True Anomaly
TOA	Time-of-Arrival
XNAV	X-ray Pulsar Navigation

Introduction

X-ray pulsar navigation (XNAV) is a celestial navigation system that uses the consistent timing nature of X-ray photons from milli-second pulsars (MSP) to perform space navigation. A visual representation can be seen in Figure 1.

Consider two observers and a single source that emits photons. At a time t, that source emits a wave front of

photons towards the two observers. Both observers locally time when the same photon wave front arrives at their location. It is assumed that the time synchronization between the two locations is of sufficient precision. With that assumption, the distance Δd between these two observers would be proportional, within a first order approximation, to the time delay t_d between both observers.

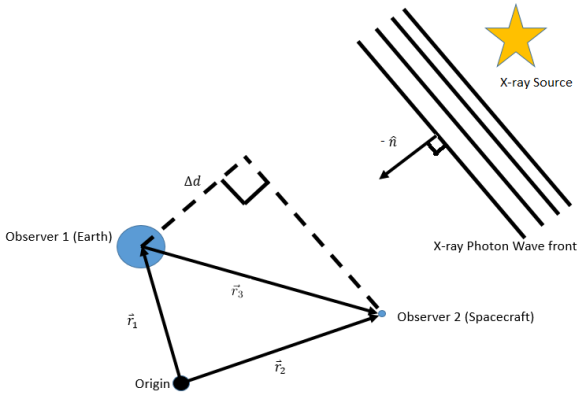

Figure 1: X-ray Pulsar Navigation (XNAV) Diagram

$$\Delta d = \hat{n} \cdot (\vec{r}_2 - \vec{r}_1) = \hat{n} \cdot \vec{r}_3 = ct_d \tag{1}$$

In the equation above, c is the speed of light, $\vec{r}_1$ and $\vec{r}_2$ are the vectors from the origin to each observer, and $\hat{n}$ is the normalized direction vector towards the source. The differenced position vector that points from Earth to the spacecraft observer is represented with $\vec{r}_3$. With successive iterations of timing comparisons, one can create range measurements. With nominally three or more X-ray sources, one can estimate the full spacecraft state.

Scope of Study

This paper presents a subset of research pulled from Reference [19]. It uses a different approach to evaluating XNAV performance compared to previous studies. It simulates photons arrivals, creates a navigation measurement with a measurement model, and then applies the measurement in a filter to estimate the state. The process follows Figure 2. In previous studies, the measurement model is directly applied without simulating photons [14] or hardware is used to simulate pulsar photon arrivals [18]. This study simulates all three steps. For simulating photon arrivals to a instrument, the National Aeronautics and Space Administration (NASA) Neutron-star Interior Composition ExploreR (NICER)/Station Explorer for X-ray Timing and Navigation Technology (SEXTANT) hardware was baselined. The NICER/SEXTANT mission is an X-ray telescope experiment that will be on the International Space Station (ISS) in 2017. Also, the trade space of this study is also limited to bounded Earth orbits. A graphical representation of the trade space can be seen in Figure 3. Table 1 shows the orbit parameter value ranges used in this study.

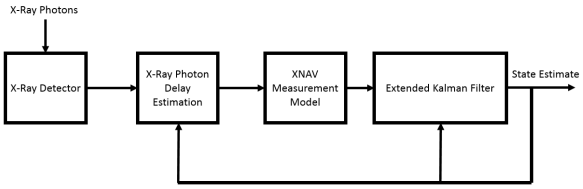

Figure 2: XNAV Navigation System Overview

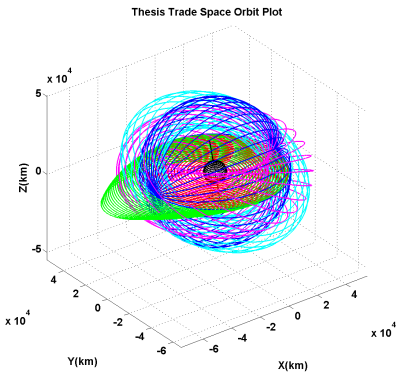

Figure 3: Orbit Design Trade Space. Different colors represent the variation of different orbital elements.

X-ray Pulsars

Pulsars are dense, magnetized, rotating neutron stars which can emit across a wide range of the electromagnetic spectrum. A subset of pulsars that have emissions in the X-ray spectrum are called Millisecond Pulsar (MSP)s. They have a relatively fast period of 1.5-16 milliseconds and have a timing stability in their emissions comparable to atomic clocks [10]. A stable timing reference is essential for navigation performance. To accurately discern timing information from the pulsar X-ray signal, the received photon wave fronts need some qualitative properties: significant intensity, stable periodic behaviors, and sharp emission profiles.

Simulating Milli-Second Pulsar Time of Arrivals

To model the timing behavior of an MSP at an X-ray detector, a representation of the photon time of arrivals must be created. With this representation, the simulation can replicate arrival photon times to generate XNAV range/range rate measurements. More details can be found in other sources such as [6].

A pulsar's photon time of arrivals at a detector is characterized by a total photon count rate function. A pulsar photon count rate is defined in Equation (3) over time t.

$$\lambda(t) \geq 0 \tag{2}$$

$$\lambda(t) = \beta + \alpha h(\phi(t)) \tag{3}$$

$h(\phi)$ is a normalized light curve function, ϕ is the detected phase within a pulsar's periodic cycle (ranging

Table 1: Orbit Trade Study Ranges

Initial Orbit Parameter	Value
Start Epoch	02/25/2017 00:00:00.000 UTC
Experimental Period	3 days
Semi-Major Axis (SMA)	6678 km - 42158 km (Low Earth Orbit (LEO) to Geosynchronous Earth Orbit (GEO))
Eccentricity (ECC)	0.0 - 0.8
Inclination (INC)	0 - 180 degrees
Argument of Periapsis (AOP)	0 - 360 degrees
Right Ascension of Ascending Node (RAAN)	0 - 360 degrees
True Anomaly (TA)	0 degrees

from 0 to 1) and α and β terms are the source and background count rates respectively.
This pulsar function $\lambda(t)$ is then utilized in a Poisson process $P(N_t = k)$:

$$P(N_t = k) = \frac{1}{k!}[(\int_0^t \lambda(x)dx)^k * e^{-\int_0^t \lambda(x)dx}] \quad (4)$$

The mean for this process is

$$E[N_t] = var[N_t] = \int_0^t \lambda(x)dx = \Lambda(t) \quad (5)$$

While the probability density function is

$$P(t_i{}_{i=1}^{M}, M) = \begin{cases} e^{-\Lambda} \prod_{i=1}^{M} \lambda(t_i) & \text{for M} \geq 1 \\ e^{-\Lambda} & \text{for M} = 0 \end{cases} \quad (6)$$

A graphical representation of photon time of arrivals and the light curve is presented in Figure 4. The pulsar light curve is plotted in red alongside associated photon time of arrivals in blue. The continued collection of photons in blue should add photon arrivals that resemble the pulsar light curve in red.

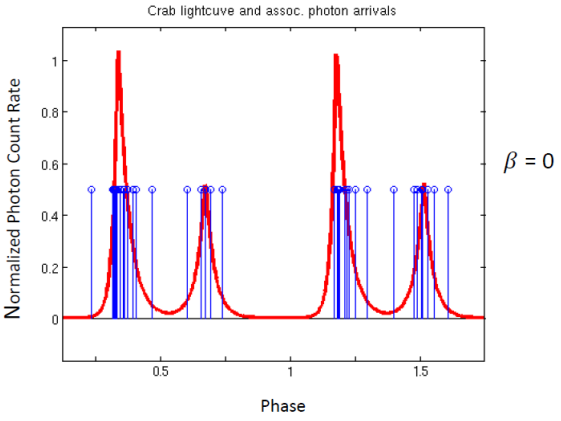

Figure 4: Light Curve function with Associated Photon Arrivals. [9]

The background rate of the curve seen in Figure 4 is 0. Increasing the background count rate means that the photon time of arrivals are measured with a higher flux. This increased flux deteriorates the correlation between the light curve and the associated photon arrivals, resulting in a deteriorated timing accuracy of the pulsar XNAV measurement.
With this stochastic process, photon arrivals for an XNAV measurement are calculated with an estimator. A metric called the Cramér-Rao lower bound (CRLB) can be used to compare estimator performance. Further definition and details about the Cramér-Rao Lower Bound (CRLB) are referenced in [6]. With XNAV, this term is used primarily to characterize how much observation time it will cost to achieve a lower bound variance of timing error in the previous model. Timing accuracy, using light time delay, is an indication of the lower bound of position state accuracy for XNAV.

Chosen MSPs Properties and Settings

Four pulsars were chosen for this study. The number and location of pulsars were chosen to provide a diverse geometric set of data to solve for a state in three dimensions. The pulsars chosen for this study were: B1937+21, B1821-24, J0218+4232, and J0437-4715. Details about each pulsar chosen for the study are shown in Table 2.
In the Earth Centered Inertial (ECI) frame, the four pulsars have unit vectors from Earth, as seen in Figure 5. Note that the targets are not evenly spread across the ECI x axis; the chosen pulsar target were a compromise between geometry, timing accuracy and other timing model properties.

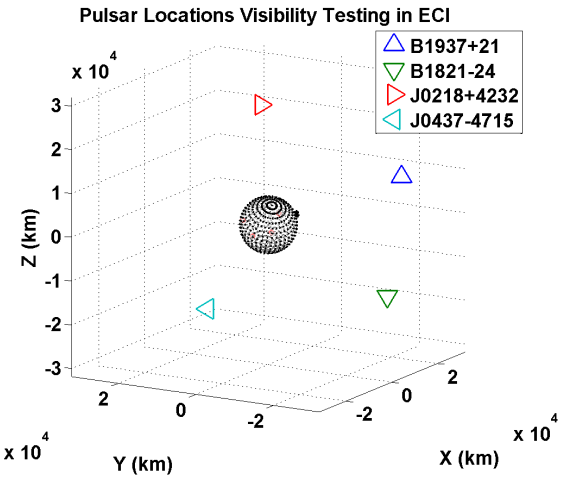

Figure 5: study Pulsar Unit Vectors in ECI

Figure 6 represents the CRLB variance versus observation time. It is the first order timing error of the pulsar model versus observation time. On the logarithmic scale, increasing the observation time on a pulsar results in the overall decrease of the standard deviation of calculating photon time of arrival. This information is based only on the analytical formulation of the CRLB

Table 2: List of Study MSP Pulsars for Navigation [18]

Name	Period (ms)	Source Pulsed Rate (α, cnts/s)	Total Bkg Rate (β, cnts/s)	TOA & Models Source	Timing Accuracy (s)	Obs Time/Meas (s)
B1937+21	1.558	0.029	0.24	PPTA	1.40e-5	1800
B1821-24	3.054	0.093	0.22	PPTA/Nançay	1.64e-5	600
J0218+4232	2.323	0.082	0.20	Nançay	6.4e-5	900
J0437-4715	5.757	0.283	0.62	PPTA	2e-4	600

and does not include hardware impacts.

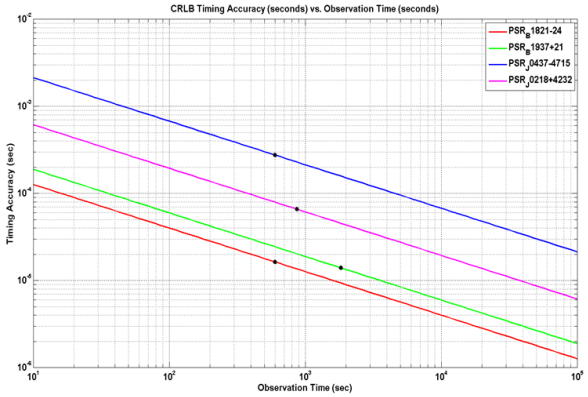

Figure 6: Source pulsars chosen and CRLB observation time

It is important to note that any point along each plot in Figure 6 can be chosen to dynamically adjust timing accuracy for navigation performance. This study fixes that value with two bounds. A lower bound of observation time was made based on providing a minimal 2e-5 second timing accuracy(an equivalent to about 5 km of position state accuracy). On the other side, observations of each pulsar were capped based on the orbital period of the trade space. Within the trade space, the smallest value of SMA equates to an orbital period of 5400 seconds. This value was the maximum observation time upper bound. With both the vertical and horizontal axis bounded, each pulsar's observation time per measurement was chosen. See Table 2 for the direct values. These values are also represented graphically by the black dots in Figure 6. Finally, the optimization process to batch and allocate photon time of arrivals and the measurement model were based on the formulations in references [14] and [18]. This study directly utilizies those formulations to translate photon time of arrivals into XNAV measurements.

Orbit and Navigation

The orbit design and navigation setup for this study was designed to characterize one to one a large subset of bounded Earth orbits. In order to do so, this section defines the orbit trade space, the force models, and the setup of the navigation filter.

The orbit force model in this study includes the conservative forces of Earth oblateness and point gravity. They and other spacecraft parameters for the study are listed in Table 3 and were used to propagate the spacecraft dynamics in the estimate and truth state:

An Extended Kalman Filter (EKF) was implemented to determine the predictive and definitive accuracy of the resultant orbit determination. For this study, the EKF measurement noise matrix **R** is directly defined by a metric called the Cramér-Rao lower bound. Nominally, the process noise matrix **Q** would also need to be adjusted for each orbit design. This study does not implement the process noise matrix in this way. Instead, a series of assumptions were made in order to equally characterize the trade space:

1. The process noise matrix Q is zeroed out.
2. The truth and estimate state force models are the same, with two body forces and the same order of higher order geopotential gravity terms.
3. The same initial state offset of 1 km SMA was made between the initial truth and estimate state.
4. The covariance initial state is set to bound the initial state offset.

Items 1 and 2 by themselves would make any navigation irrelevant, as the estimate state's dynamics on board the spacecraft would always match the truth state for all time. Item 3 ensures error growth between the estimate and the truth. With items 2 and 3, the filter will be forced to use XNAV measurements over the estimate propagator. Item 4 ensures that the filter will recognize a need to make a correction. With these four items, the filter relies purely on XNAV measurements for any state estimation convergence.

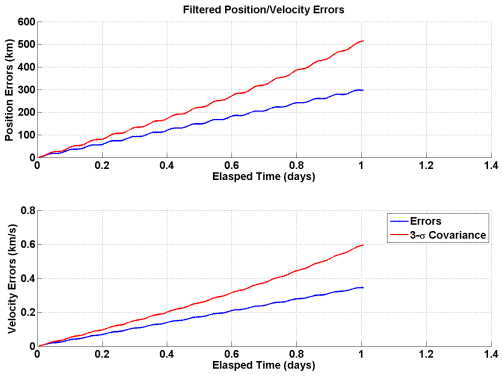

Figure 7: Navigation performance at a 300 km altitude circular orbit with no applied measurements

As seen in Figure 7, a scenario that does not apply any XNAV measurements will deteriorate. The blue line indicates the actual error between truth/estimate states while the red line indicates the filter's knowledge of that error within the covariance. As the covariance carries the variance of both position and velocity in its diagonal, the red line represents the 3σ covariance

Table 3: List of Spacecraft Parameters

Spacecraft Parameter	Value
Spacecraft Mass	800 kg
Force Model: Primary Body	Earth
Force Model: Gravity Field Degree	30
Force Model: Third Body Point Masses	None
Force Model: Solar Radiation Pressure	None
Force Model: Tidal Forces	None
Force Model: Atmospheric Drag	None

value. For both position and velocity estimates, the error within the simulation has a dominant linear increase in error, with slight sinusoidal behavior due to the higher order gravity terms. The XNAV measurements are the focus on the study and are the only driver of any navigation convergence.

XNAV Hardware

To better characterize the application of XNAV, the infrastructure of the NICER/SEXTANT mission was simulated for this study. It provides a grounded representation of XNAV performance on an upcoming mission. Note that these models are idealized and are a restriction on potential XNAV performance.

NICER/SEXTANT Overview

NICER is a NASA explorer mission of opportunity whose purpose is to study gravitational, electromagnetic, and nuclear physics environments within neutron stars. NICER and it's software enhancement SEXTANT will be launched on a SpaceX rocket to be an on board payload on the ISS in 2017 [11]. See Figure 8 for a general image and location of instruments. It is approximately a 1 m^3 telescope array.

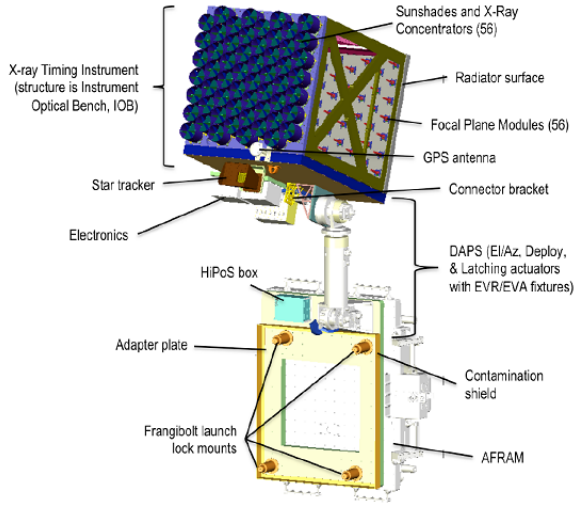

Figure 8: NICER Instrument Image. Concentrator optics are in blue which will be mechanically pointed towards each pulsar target [8].

The NICER design is made in order to reject the local background radiation with each of the 56 X-ray telescopes. In the process, it also must rotate to point to each individual pulsar target to tag pulsar Time-of-Arrival (TOA) to within its 100 nanosecond resolution. The SEXTANT technology demonstration is a flight software enhancement to the NICER instrument, funded by the NASA Space Technology Mission Directorate (Space Technology Mission Directorate (STMD)). The team will use the same data stream as NICER to perform XNAV-only orbit determination.

Hardware Implementation in Study

NICER is a science mission that, with the SEXTANT mission enhancement, is an example of an XNAV instrument. Though it is not optimized specifically for XNAV, it is an instrument that encompasses challenges inherent in maintaining appropriate timing resolution for XNAV [18] [1]. The simulation used for the study is a heavily redesigned SEXTANT simulation that can handle the trade space outside of the SEXTANT LEO orbit design. There are also several assumptions about the hardware. They include:

1. The instrument is not on the ISS, but a generalized Earth orbiting spacecraft.
2. The instrument collects X-ray photons from only one pulsar target at a given epoch.
3. Slew is modeled in the design of the pulsar observation schedule as a constant velocity with no hardware obstructions.
4. The pulsar observation schedule is generated before running the filter state estimate using that schedule.
5. The hardware is capable of handing the environment of the studied orbit trajectory.

Test Overview

The study utilizes a full end to end simulation to assess XNAV performance. It sets up the scenario a priori and then simulates XNAV measurements to evaluate performance.

As seen in Figure 9, the simulation utilizes tools (represented as blue boxes) and data products (represented as gray boxes). The orbit truth ephemeris is first generated in the mission design tool. This study uses the

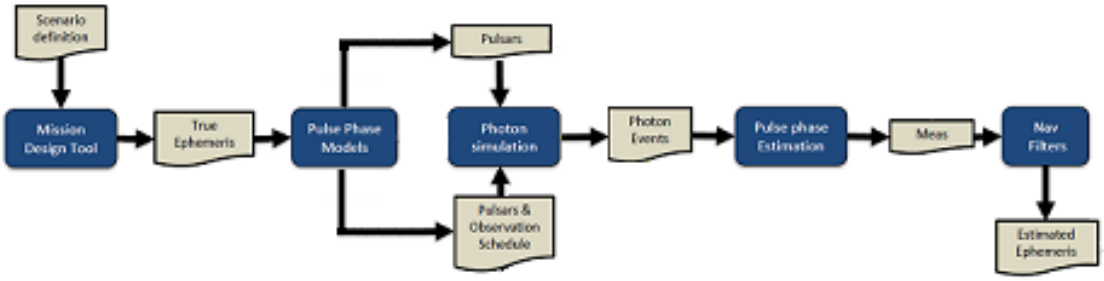

Figure 9: Simulation Infrastructure [17]

NASA open source orbit propagation software called General Mission Analysis Tool (GMAT). Using the ephemeris, the pulse phase models block extrapolates pulsar information from a database using open source software called TEMPO2 [5]. The background radiation environment throughout the projected spacecraft trajectory is also calculated in this section. At the same time, internal software is used to calculate pulsar visibility and generate an observation schedule. Once the orbit design/pulsar phase model products are produced, the simulation runs the XNAV measurement process to simulate photon events and create measurements. The measurements are applied to a running EKF and the navigation performance is recorded.

Designed for this study, software algorithms that are critical to an Earth orbit trade space design are further explored in the following sections. These include the visibility models, the background radiation model, and the scheduling algorithm that optimizes navigation performance.

Pulsar Visibility

An XNAV measurement is based on collecting photon TOAs. This process requires an observation time on each pulsar based on the CRLB. Due to the significant observation time, the XNAV process is subject to physical blockages between the detector and the pulsar. This study checks for occultations for each ephemeris time step from celestial occultations and from areas with extreme background radiation.

The driving occultations are from celestial bodies. This study models occultations from the Sun, Earth, and Moon. See Figure 10.

The other area of occultation applied in this study were areas with highly variable background radiation. Areas with too variable of a background rate in the spacecraft's immediate area were considered occulted. The South Atlantic Anomaly (SAA) at orbit altitudes around 300-1000 km as well as areas around the magnetic north and south poles have this variation in background radiation(see Figure 11).

To avoid these areas, the SAA and areas around the magnetic poles are restricted by a longitude/latitude box. Restricts were applied at orbit altitudes between 300-1000 km, while the magnetic pole areas were enforced for any orbit altitude. With these background occultations, all the pulsars were considered occulted when the spacecraft orbit enters these regions. The geometry used for these structures comes from the National Oceanic and Atmospheric Administration (NOAA) geomagnetic map reference [4] [13]. Other areas around Earth were scaled in background radiation, detailed in the next section.

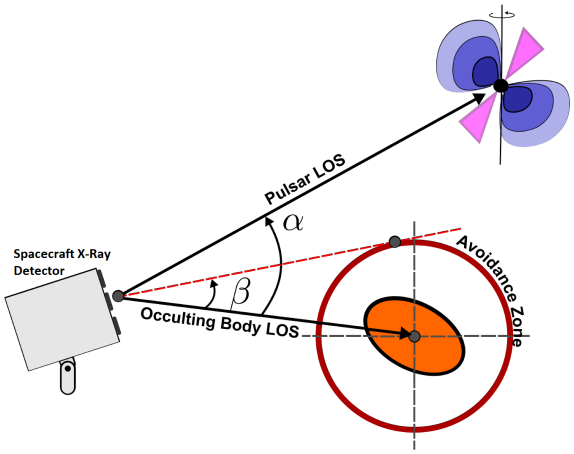

Figure 10: Celestial Body Occultation Model

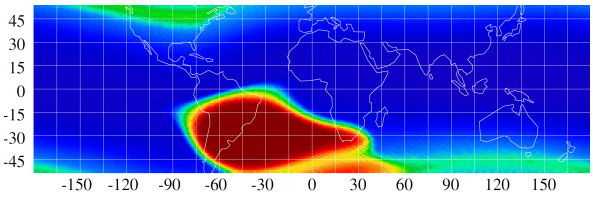

Figure 11: Background Radiation Environment around 400 km altitude versus Geodetic Longitude/Latitude (degrees). Note the high concentration areas around the South Atlantic as well as the magnetic poles [12].

Background Radiation Environment

The Earth's background radiation environment consists of two dominating radiation structures around Earth called the Van Allen belts. They are two bands of high energy levels that exist within 10 Earth radii from the Earth's center [15].

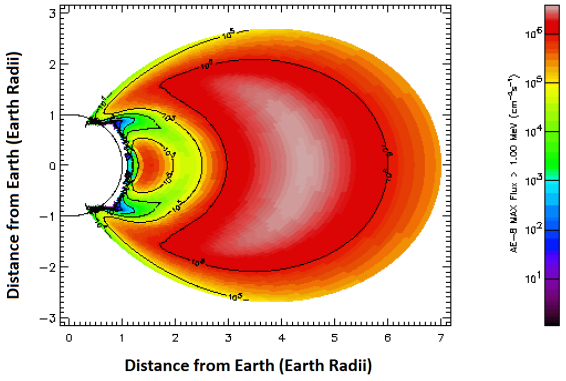

Figure 12: Background Radiation Electron Environment from the Earth surface to 7 Earth Radii. Heat plot is scaled for electron flux greater than 1 MeV. Uses Data from the AE-8 model at solar maximum [7].

As seen with this high energy map in Figure 12, two areas between 1-2 Earth radii and 3-5 Earth radii have significantly higher concentrations of electrons than other areas. With the significant variation in background environment, this study models the background environment based on the primary Van Allen Belt structures. See Figure 13 for a logarithmic plot used in the study. The horizontal axis is the spacecraft altitude at the equator in Earth radii, while the vertical axis represents the AE-8 model of electron flux at solar maximum that is greater than 100 MeV per centimeter squared seconds. A reference electron flux is marked in the simulation at 0.1 Earth radii. The other values on the plot are scaled relative to the flux at that value. For a given spacecraft state, a corresponding amount of background radiation is applied to the photon simulation and navigation measurement generation.

This application makes the assumption that the hardware will be able to handle these environments. The hardware will provide appropriate background rejection in order to effectively detect X-ray photon arrivals from individual MSP sources. One hardware example to encourage background rejection is to focus the X-ray detector on one pulsar at a time. The consequences of this assumption means that an observation schedule must be produced a priori.

Pulsar Observation Scheduling

In order to receive pulsar X-ray photons, observations of individual pulsars need to be prioritized. It takes a significant period of observation time to make a navigation measurement, so scheduled observations must be evaluated to ensure that they are effective for XNAV. With the hardware assumptions built into this study, this also requires that one pulsar is observed at a time

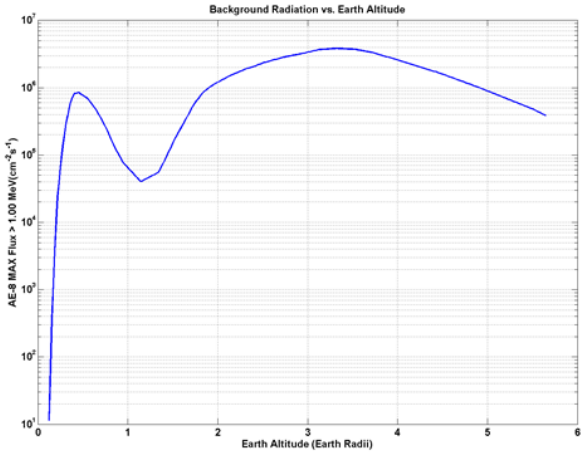

Figure 13: Background Radiation Electron Environment versus Distance from Earth. Uses Data from the AE-8 model at solar maximum [16].

and that the schedule is produced before the EKF solution is simulated. To address these issues, a scheduling algorithm was designed for this study.

The schedule algorithm builds a schedule by appending immediate observation schedules to a final schedule product. It creates multiple immediate schedules that comprise of a subset of the full simulation period. It then evaluates their metric and chooses the ideal schedule. This continues until the end of the simulation period.

An immediate schedule is created by traversing forward in time through both visibility and ephemeris data, scheduling pulsar observations focused on making a measurement for a particular pulsar. Multiple possible schedules are created in the process; for N pulsars, there are N immediate schedules. Observations are scheduled up until an XNAV measurement on that pulsar can be created, based on the the CRLB analysis described earlier. If that chosen pulsar is occulted but more observation time is required, the pulsar with the smallest observation time based on the CRLB is chosen instead for observation.

Once these immediate schedules are produced, the scheduling algorithm then uses a local greedy heuristic to pick a schedule to append to the final observation schedule. That schedule is chosen using a covariance based analysis. Looping through each immediate schedule, the algorithm calculates (or initializes) the covariance matrix (P_i^-), the state transition matrix (Φ), and the spacecraft state at the current simulation time t_0. Next, the previous covariance P_{i-1} is then propagated up to the first measurement time made from an immediate schedule called t_i.

$$P_i^- = \Phi(t_0, t_i) P_{i-1} \Phi(t_0, t_i)^T \tag{7}$$

Once the covariance is propagated to the measurement time (P_i^-), a Kalman gain is updated based on the covariance. This also uses the relevant measurement noise

from the pulsar R_i.

$$K_i = P_i^- H_i^T [H_i P_i^- H_i^T + R_i] \tag{8}$$

The covariance is then updated with the given measurement.

$$P_i = [I - K_i H_i] P_i^- \tag{9}$$

If more than one measurement was made with the immediate schedule, the process is repeated. The algorithm then evaluates a metric based on the covariance matrix to determine which schedule to choose. Based on past research [3] [2], the criteria of this scheduling algorithm is to minimize the projected SMA variance. This is done with a partially differentiated vis viva equation (Equation (10)) with respect to position magnitude r and velocity magnitude v. As reference, the formulation is listed below:

$$\frac{-\mu}{2a} = \frac{1}{2}v^2 - \frac{\mu}{r} \tag{10}$$

$$\delta r = \frac{1}{2}\left[\frac{(2\mu - rv^2)^2}{\mu^2}\right]\delta a \tag{11}$$

$$\delta v = \frac{1}{2}\left[\frac{(2\mu - rv^2)^2}{\mu r^2 v}\right]\delta a \tag{12}$$

The algorithm then loops through all the immediate schedules until all of the SMA variance metrics have been calculated. The algorithm then finds the immediate schedule with the lowest variance and appends it to the final schedule output. The covariance that came with the schedule is saved and the process is continued to find the next pulsar measurement. This repeats until the end of the simulation period.

A flow diagram of the entire process can be seen in Figure 14. As seen in that flow diagram, the terms "immediate" and "feasible" are used interchangably.

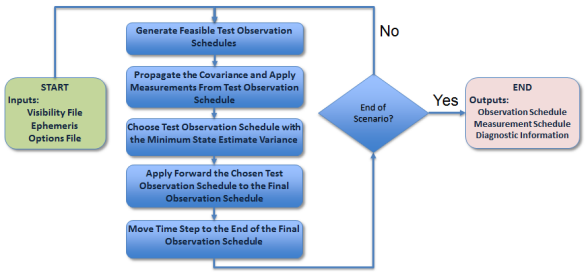

Figure 14: Pulsar Scheduling Flow Diagram

An example representation of pulsar visibility and the resultant schedule is seen in Figure 15. The horizontal axis represents the elapsed time in days. The vertical axis shows the visibility plot as seen in earlier sections, with each line representing the visibility of each pulsar. Observations are scheduled in a separate color on top of these visibility periods, shown in cyan. Finally, the black X indicates where a pulsar measurement from that pulsar is generated.

Results

This section details the results of XNAV performance based on varying individual kepler elements. It details how the filter performance was measured. The following sections then detail the hard data results.

In terms of measuring performance of the filter, two primary post processing metrics are used to quantify the navigation influence of XNAV measurements. One is the definitive state error, the difference between the state and its estimate over time. The second metric used is the definitive state error transformed into the equivalent value of SMA. SMA has the unique property of being the primary driver of specific orbital energy, a strong predictor that the definitive state error will converge [3].

There are also two common metrics that are observed as they are common symptons of the eventual navigation performance: the visibility of the pulsar over the given observation period and the photon phase residual.

Visibility is a critical resource for that drives XNAV measurement frequency and quality. If the breakup in visibility is too great, the collection of photon TOAs are broken up over multiple periods of visibility. The resultant formulation then loses information from the phase estimation process. The ideal visibility for XNAV would allow photon TOAs to be collected in one continuous period where the spacecraft's average velocity would be minimal. The phase residual is calculated by differencing the expected signal phase from the TEMPO2 software with the simulated phase of photon TOAs at the X-ray detector. If the phase residual is over an expected 3σ bound, it is edited out. This is because the subsequent residual phase is within a single cycle of pulsar emissions. Over a certain threshold, a given residual may be greater than a single cycle and is thus edited out (see Equation (3)). XNAV performance deteriorates with more and more edited measurements.

Single Kepler Element Variation

By varying one kepler element with the trade space, the impact of the spacecraft orbit can be seen with tracking XNAV performance. Terminology used in the subsequent plots are defined in this section.

The averaged definitive state error is the primary metric. The definitive state error is the state error difference measured at a specific time of the simulation. It is designated as definitive as it does not provide any information about the projected error growth of the filter estimation. Once calculated, this error is averaged over the final day of the simulation. This period was chosen to represent the steady state behavior of the state estimate.

Visibility is averaged in two different ways. The continuous visibility average is the average between every period of visibility that is unbroken by an occultation. This average was chosen to see if a pulsar XNAV measurement can be made within one visibility period. Any breakup in observations for a measurement results in a decrease in measurement accuracy, which increases the chance a measurement will be removed. The second

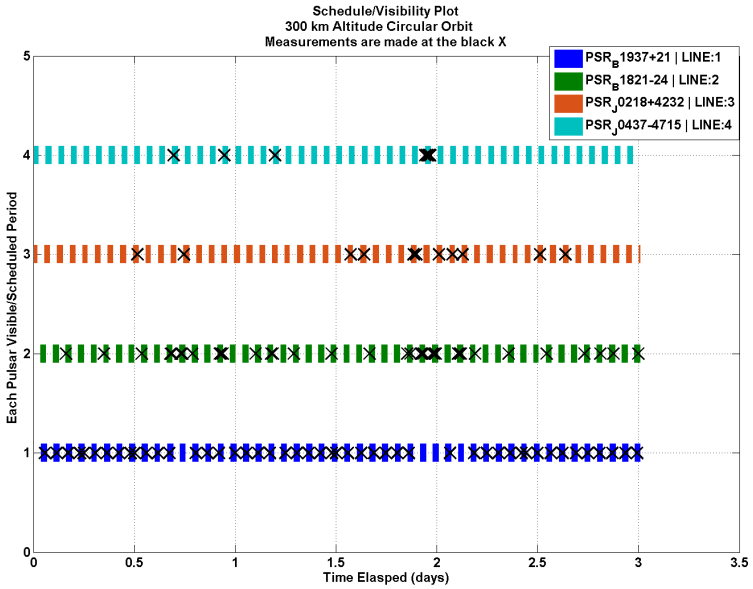

Figure 15: Example of a Pulsar Schedule Overlay to a Visibility Plot

visibility average is the average visibility per orbital period. Both summarize the continuity of individual periods and the frequency they appear relative to the orbit dynamics.

Measurement quality is determined by the total number of measurements and percent of measurements removed. The total number of measurements is the total number of measurements that were generated in the simulation. The percentage of measurements removed records the ratio of rejected over total measurements due to the phase residual limits. Both numbers are needed to determine the total number of XNAV measurements used in the EKF.

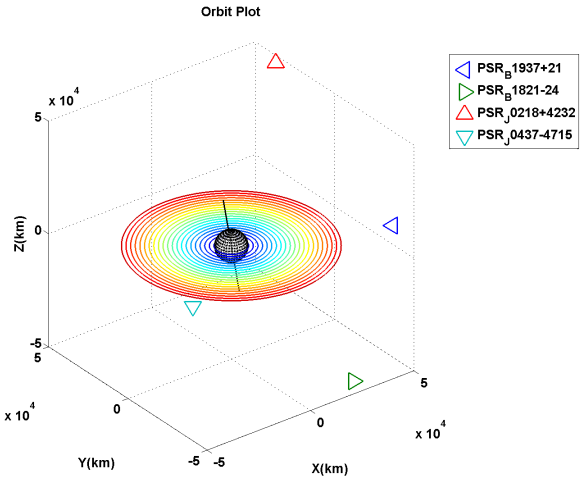

Figure 16: SMA Orbit Trade Space. Orbit trade value increases from blue (6678 km) to red (42158 km) for each trajectory.

Variation of Orbit Semi-Major Axis

Figure 16 is a graphical representation of the orbit trade space with SMA. XNAV performance over varying semi-major axis is represented in Figures 17, 18, and 19. The nominal orbit parameters have an eccentricity of 0 and an inclination of 0°. As the orbit is circular and equatorial, argument of periapsis/RAAN are not formally defined.

For definitive state error and the definitive state semi-major axis error, the lowest value in the trade space of 6678 km semi-major axis had an average position error above 5 km and an average velocity error above 0.005 km/s. The rest of the semi-major axis trade space stays below those values. The orbit design has the most influence on the lowest value of semi-major axis, and averages out for the rest of the trade space. There is also an increase in the definitive position error that peaks in the middle of the trade space (25000 km semi-major axis).

The measurement quality can be seen in Figure 18. A peak percentage of measurements (around 30%) are edited out around an semi-major axis of 25000 km, just like the peak in state error averages. The number of measurements increases with semi-major axis until a value of 300 measurements around 20,000 km semi-major axis. At this point, the total number of measurements remains +/- 50 measurements off that nominal value for the rest of the trade space.

Finally, increasing semi-major axis increases visibility of all pulsars. With increasing semi-major axis, each pulsar increases visibility at a different linear slope. With the geometry seen in Figure 16, pulsar J0437-4715 always has visibility on the spacecraft after a certain threshold of semi-major axis. The visibility for that pulsar peaks at about 4320 minutes, or the full simulation time of three days.

The increase of semi-major axis significantly increases the visibility of all pulsars. The increase in visibility

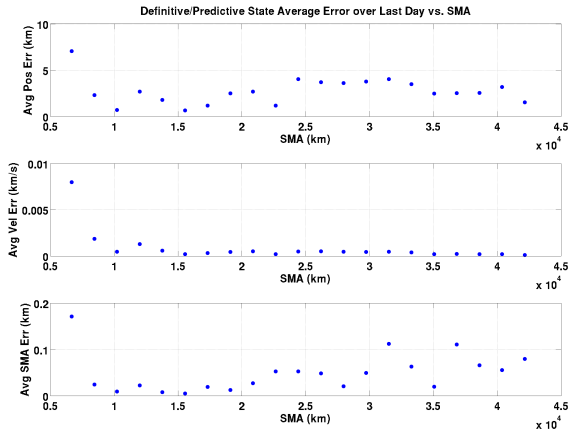

Figure 17: Average State Error vs. SMA. Equatorial Circular Orbit.

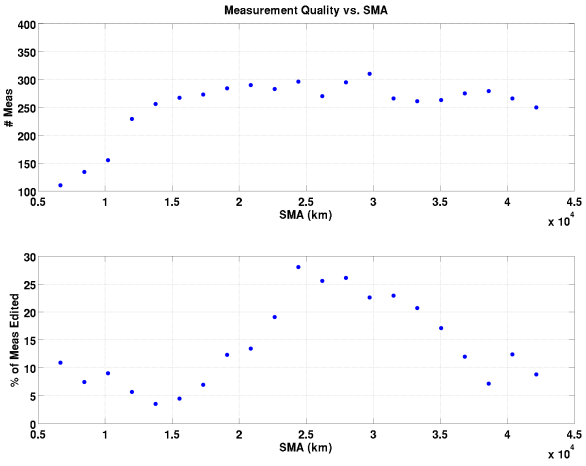

Figure 18: Measurement Quality vs. SMA. Equatorial Circular Orbit.

allows the scheduling to maximize the number of XNAV measurements throughout the simulation. That maximum is reached around 20,000 km semi-major axis. At the same time, an increase in background radiation peaks between 20,000-25,000 km in Figure 13. This corresponds to the increase in edited measurements and the increase in the state error plot. As a result, it is generally favorable to increase semi-major axis beyond 40,000 km semi-major axis. This allows the maximum number of XNAV measurements while decreasing the total number of rejected measurements. It also equates to low definitive state error averages while avoiding areas with high background radiation.

Variation of Orbit Eccentricity

Figure 20 is a graphical representation of the orbit trade space with ECC. XNAV performance is shown in Figures 21, 22. The nominal orbit parameters have an semi-major axis of 42158 km, an inclination of 0°, and an argument of periapsis at 0°. This set of orbits will be equatorial, so right ascension of the ascending node will be undefined.

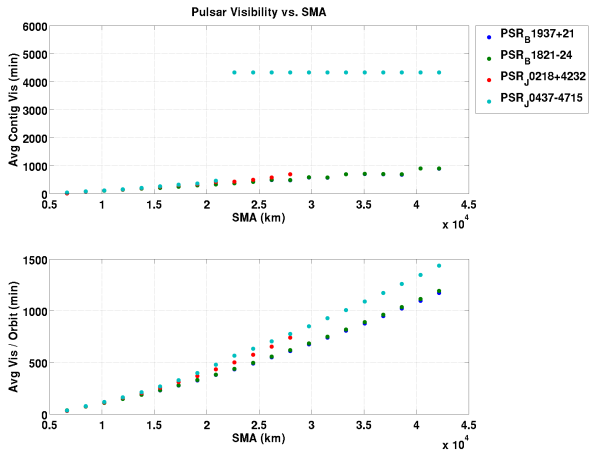

Figure 19: Average Visibility vs. SMA. Equatorial Circular Orbit.

As seen in Figure 21, the average position and velocity

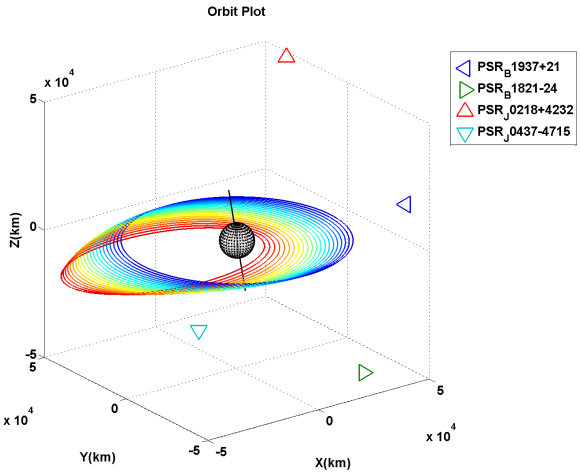

Figure 20: ECC Orbit Trade Space. Orbit trade value increases from blue (0) to red (0.8) for each trajectory.

error averages has an upper bound of 10 km and 0.8 m/s, respectively. The position and velocity averages has a lower bound of 1.9 km in position error and 0.15 m/s velocity error, respectively.

There are a couple of trends that exist within the eccentricity definitive error plots. The position error and velocity error averages increase between an eccentricity of 0.2 and 0.6. At an eccentricity of 0.6, the definitive state error for both position and velocity drops sharply. Increasing eccentricity past 0.6, the error begins to grow again in both position and velocity. Increasing eccentricity past 0.6 also shows an increase in the averaged semi-major axis definitive error.

As seen in Figure 22, there is a fluctuation in total number of measurements and the edited measurements. The maximum rejected number of measurements is around 10%, and the total number of measurements can peak up to 350 measurements. As seen in Figure 22, the increase of eccentricity is related to a downward periodic trend of total XNAV measurements. At 0.2, 0.4 and 0.6 eccentricity, the total number of

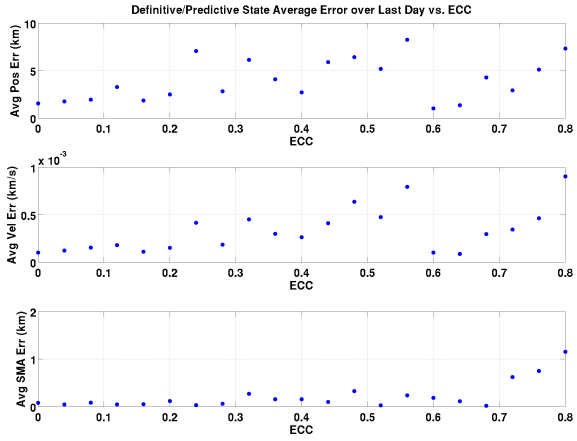

Figure 21: Average State Error vs. ECC. 42158 km semi-major axis Equatorial Orbit.

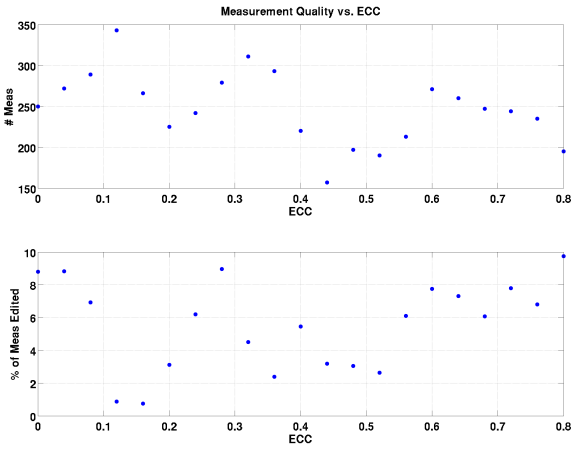

Figure 22: Measurement Quality vs. ECC. 42158 km SMA Equatorial Orbit.

measurements reaches a local minimum. At the same time, increases in edited measurements occur between 0.2-0.3 eccentricity and after 0.5 eccentricity. Together, the total number of used XNAV measurements peaks between 0.1 and 0.2 eccentricity, while the other values of eccentricity show a drop in used XNAV measurements.

Seen in Figure 23, visibility has a significant drop between values of 0.1 and 0.6. The visibility averages double in value beyond 0.6 eccentricity.

In summary, an eccentricity up to 0.2 has some minor benefits to XNAV performance. Increasing eccentricity shows an increase in visibility and total measurements while decreasing rejected measurements. Even though the definitive average error in position, velocity, and semi-major axis stay at a lower value up to 0.2 eccentricity, the pulsar visibility and total number of measurements drop between 0.1 and 0.2 eccentricity. Beyond 0.2 eccentricity, a growth in definitive state error is observed. The return of pulsar J0437-4715 visibility at an eccentricity of 0.6 equates to the sudden jump in total measurements and thus definitive average error. Increasing eccentricity past

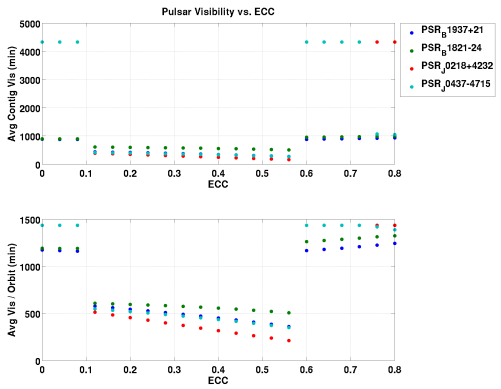

Figure 23: Average Visibility vs. ECC. 42158 km SMA Equatorial Orbit.

0.6 decreases the total measurements and the number of rejected measurements, which brings up all the averages of definitive state error.

Variation of Orbit Inclination

Figure 24 is a graphical representation of the orbit trade space with INC. XNAV performance over varying inclination is shown in Figures 25, 26, and 27. The nominal orbit parameters have an semi-major axis of 42158 km, an eccentricity of 0, and a right ascension of the ascending node at 0°. argument of periapsis is undefined for a circular orbit.

The variation of inclination shows an averaged state

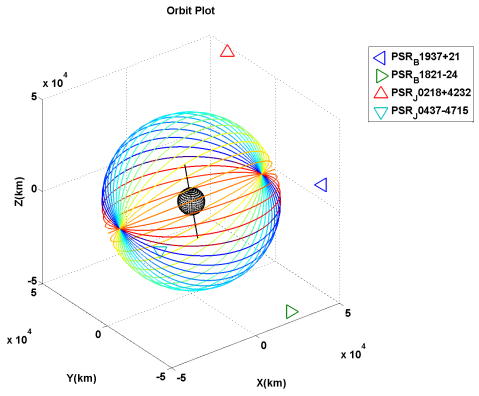

Figure 24: INC Orbit Trade Space. Orbit trade value increases from blue (0°) to red (180°) for each trajectory.

error below 6 km Root Sum Square (RSS) in position, 4.2e-4 km/s in velocity, and 0.4 km for SMA estimation for the entire trade space. There is a maximum average state error in all plots of Figure 25 near 90° INC.

There is a drop in total measurements and an percentage increase in edited measurements around 90° INC, as seen in Figure 26.

The visibility averaged periods between an inclination of 60°and 160° suddenly drops for continuous periods but not for orbital periods. Also, pulsar J0427-4715 is visible for the entire three day scenario between an inclination of 25° and 50°.

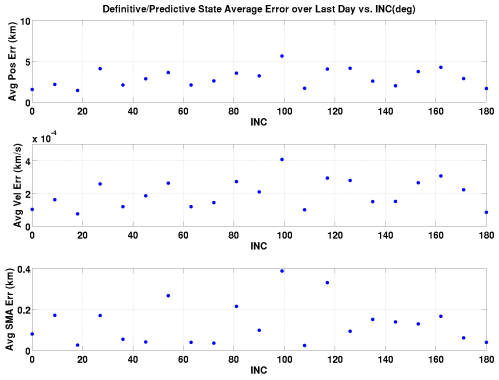

Figure 25: Average State Error vs. INC. 42158 km SMA Circular Orbit.

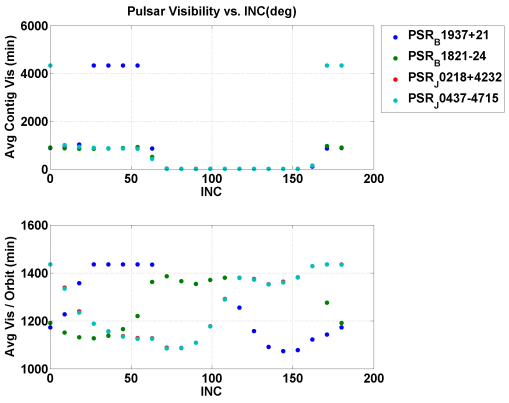

Figure 27: Average Visibility vs. INC. 42158 km SMA Circular Orbit.

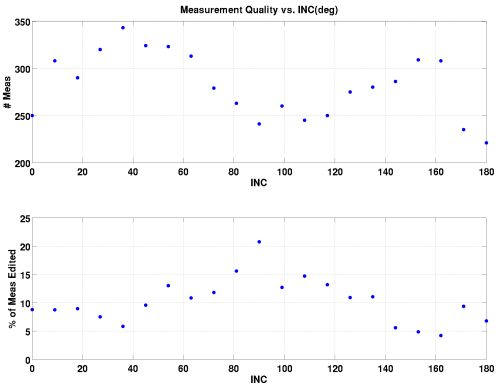

Figure 26: Measurement Quality vs. INC. 42158 km SMA Circular Orbit.

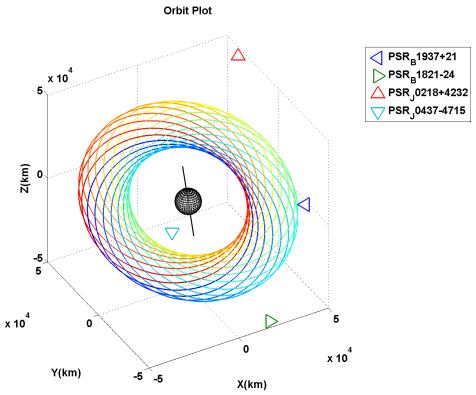

Figure 28: AOP Orbit Trade Space. Orbit trade value increases from blue (0°) to red (360°).

Areas near the magnetic north pole and south pole were treated similarly to occultations due to the significant variation of background radiation. As a result, orbits with an inclination around 90° spend more time passing over these poles, during which all pulsars are occulted. This causes the sudden drop in visibility and thus a lower drop in total measurements. With the breakup of observations due to the magnetic pole occultations, the percentage of edited measurements increased as well. As a result, the averaged definitive state error increased to 6 km in position, 4.1e-4 km/s in velocity, and 0.391 km in definitive semi-major axis error.

Variation of the Orbit Argument Of Periapsis

Figure 28 is a graphical representation of the orbit trade space with AOP. XNAV performance versus argument of periapsis is shown in Figures 29, 30, and 31. The nominal orbit parameters have an semi-major axis of 42158 km, a eccentricity of 0.3, an inclination of 28.5°, and a right ascension of the ascending node at 0°.

The argument of periapsis trade in Figure 29 shows a maximum averaged position error of 4.5 km and a maximum averaged velocity error of 4e-4 km/s. The definitive semi-major axis error is bounded to 0.3 km error. The semi-major axis error indicates periodic increases about every 65° with various amplitudes. There is a general decrease in XNAV measurements from 0° to 150°. A maximum of XNAV measurements appears between 150° and 200°. There is also a repeated pattern in rejected measurements between 0° to 150°. Higher values of argument of periapsis beyond 150° are varied in quality.

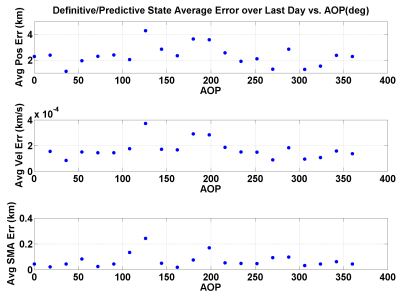

Figure 29: Average State Error vs. AOP. 42158 km SMA Eccentric Inclined Orbit.

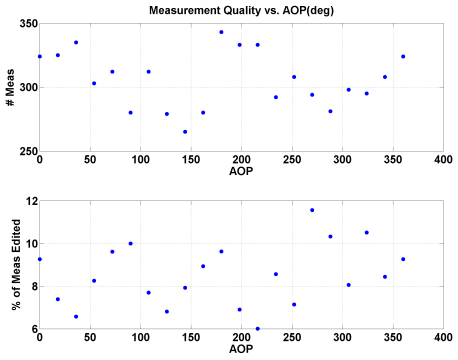

Figure 30: Measurement Quality vs. AOP. 42158 km SMA Eccentric Inclined Orbit.

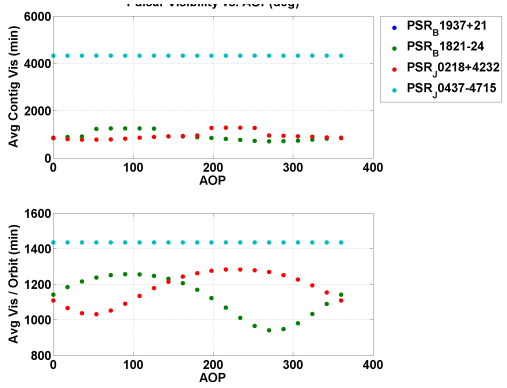

Figure 31: Average Visibility vs. AOP. 42158 km SMA Eccentric Inclined Orbit.

Pulsar visibility shows the most pronounced pattern based on argument of periapsis. Pulsar B1937+21 and J0437-4715 are visible for the entire trade space, and the other two pulsars sinusoidally vary in visibility throughout the scenario.

The orbit geometry reveals more about XNAV performance and argument of periapsis. The greatest build-up of definitive state error is in the in-track direction of the Radial, In-track, Cross-track Spacecraft-fixed Rotating Reference Frame (RIC) frame [2]. As this component is consistently in the orbit plane, finding an orbit plane that is aligned with the pulsar unit vector allows the photon pulsar information from that target to address the worst local direction of definitive state error.

Besides that observed pattern, information on the XNAV performance based on argument of periapsis is limited based on the current data. For a given value of semi-major axis, eccentricity and inclination in the trade space, the total rate of change of right ascension of the ascending node and argument of periapsis varies significantly over time. A secular precession of the orbit plane requires appropriate information to perform orbit determination. If there is less out-of-plane orbit motion, the XNAV measurements will not need to estimate that motion. Further study of the argument of periapsis trade space would need to study the relationship of timing accuracy, the scheduling algorithm, and the relative orbit geometry of the pulsar targets. As the measurements are scheduled sequentially, the analysis of argument of periapsis with encompassing all possible groups of XNAV measurements is non-trivial.

Variation of the Orbit Right Ascension of the Ascending Node

Figure 32 is a graphical representation of the orbit trade space with RAAN. XNAV performance versus right ascension of the ascending node is shown in Figures 33, 34, and 35. The nominal orbit parameters have an semi-major axis of 42158 km, a eccentricity of 0.3, an inclination of 28.5°, and an argument of periapsis at 0°.

RAAN does not show as strong of periodic behavior

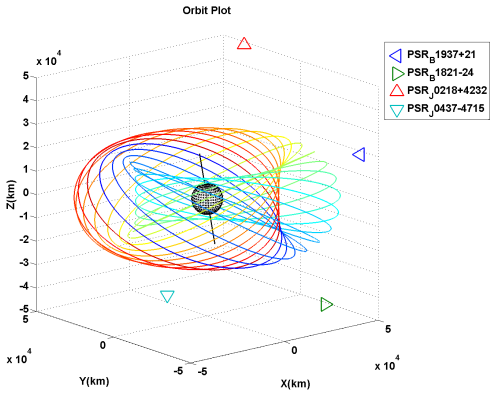

Figure 32: RAAN Orbit Trade Space. Orbit trade value increases on from blue (0°) to red (360°) trajectories.

of argument of periapsis, but the state error averages for right ascension of the ascending node are capped by the same limits as the results across argument of periapsis. There is a peak of definitive state error between 200° and 250° RAAN.

Seen in Figure 34, the total number of XNAV measurements stay around 270 measurements between 50°and 200° RAAN. For a value of right ascension of the ascending node greater than 200°, the total number of XNAV measurements vary by +/- 100 measurements.

As seen in Figure 35, pulsar J0437-4715 has almost constant visibility except from 50°to 200°. B1821-24 is fully visible for the entire scenario for a right ascension

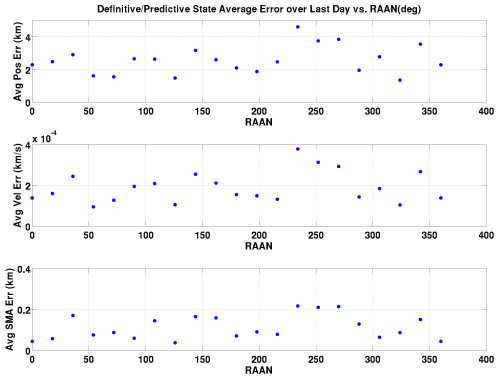

Figure 33: Average State Error vs. RAAN. 42158 km SMA Eccentric Inclined Orbit.

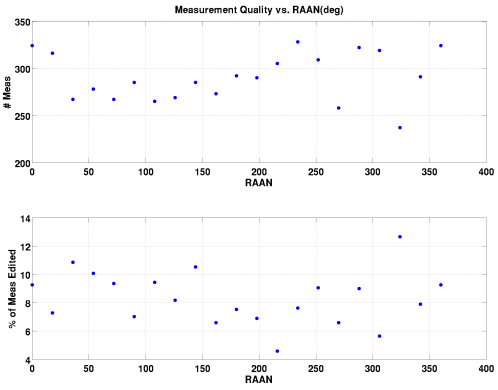

Figure 34: Measurement Quality vs. RAAN. 42158 km SMA Eccentric Inclined Orbit.

of the ascending node between 200° and 250°. Each pulsar has a unique trend of pulsar visibility averaged over and orbit period. As per the definition of the three orbit rotation angles right ascension of the ascending node, argument of periapsis, and inclination, the pattern is periodic over the entire trade space. For right ascension of the ascending node, the pattern is less sinusoidal than the other orbit parameters. The sudden drop in visibility is due to the orbit geometry and the change of right ascension of the ascending node.

Overall, the conclusions for XNAV performance versus right ascension of the ascending node is similar to the study of argument of periapsis. Future work is needed to define the relationship between the pulsar timing accuracy, geometry of XNAV measurements and the scheduling algorithm. Finally, XNAV definitive state error with varying right ascension of the ascending node is on the same order of magnitude as argument of periapsis, so right ascension of the ascending node seems to have a small influence on averaged state errors as does argument of periapsis.

Sensitivity of Initial Conditions

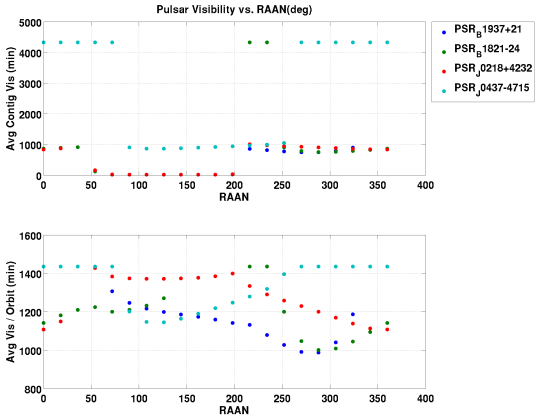

Figure 35: Average Visibility vs. RAAN. 42158 km SMA Eccentric Inclined Orbit.

It has been observed that initial measurements of XNAV dictate a large part of XNAV performance with this study. One way to observe this behavior is to track an orbit with a small value of semi-major axis, as the total amount of pulsar visibility per orbit shortens. With an eccentricity of 0 and an inclination of 0°, the right ascension and the argument of periapsis will drive which pulsars will be available for observation. This is a discrete way to change the cadence of measurements and thus navigation performance.

Figures 36, 38, and 40 show that performance can change from convergence to divergence with the change of argument of periapsis and right ascension of the ascending node. With Figure 37, 39 and 41, the schedules are significantly different. The initial measurement of B1821-24 results in navigation convergence, while the initial measurement of another pulsar caused by a different right ascension of the ascending node results in divergence.

This particular formulation of XNAV makes a significant number of linearity assumptions. In the process, it has a sensitivity to the total number of pulsar measurements over a given time period. As the state will deteriorate without any XNAV measurements, subsequent state estimate updates from XNAV measurements must be frequent enough to assert that the orbit dynamics can still be linearized. This requirement is seen in multiple places of the XNAV formulation. First, the pulsar phase estimation detailed in Reference [18] involve the optimization of phase and frequency offset coefficients. The formulation requires short pulsar observation periods since the coefficients model a linear equation. This linearization is, to first order, related to the offset of state accuracy in the direction of the pulsar. If a linear estimate cannot be found to perform phase estimation, the XNAV measurement is less accurate for state estimation. Second, the measurement model for XNAV from Reference [18] requires an estimate state a-priori to update said estimate. If a series of inaccurate estimate states (from inaccurate measurements) are used in the measurement model, the solution will naturally

diverge. Finally, an EKF is formulated by linearizing around the estimate state. If estimate states in the EKF cannot be related to each other by the linear transformation of the state transition matrix, the filter itself will also fail to estimate the spacecraft state.

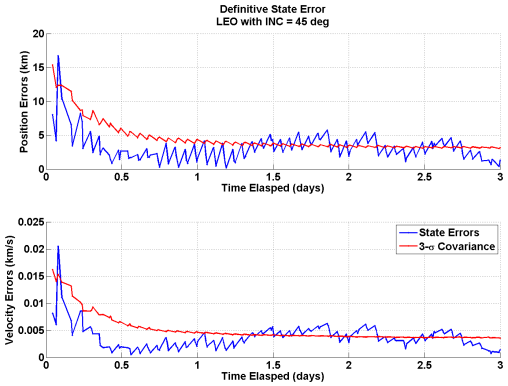

Figure 36: Definitive Error performance for a LEO with an INC of 45°with AOP and RAAN equal to 0°.

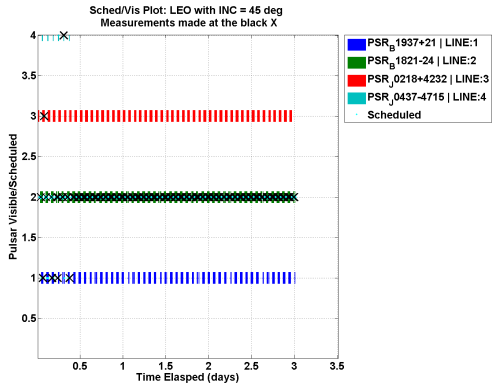

Figure 37: Pulsar Visibility/Schedule for a LEO with an INC of 45°with AOP and RAAN equal to 0°.

Conclusions

Initial orbit parameters of closed Earth orbits are an indicator of XNAV performance in terms of pulsar availability, the background radiation environment and the resultant spacecraft dynamics. The results of this study show a sensitivity of the EKF state estimate performance based on the resultant cadence of XNAV measurements. That cadence is a result of pulsar availability and the measurement quality, whose behavior is a result of spacecraft dynamics and ambient background radiation.

The majority of orbits can be tracked with XNAV measurements to within no more than 10 km position error, worst direction, in the 3 day experiment period. If the orbit parameters are restricted to a particular subset, this can improve to no more than 5 km position error, worst direction, over 1 day. This section summarizes the influences that each orbit parameter has on XNAV

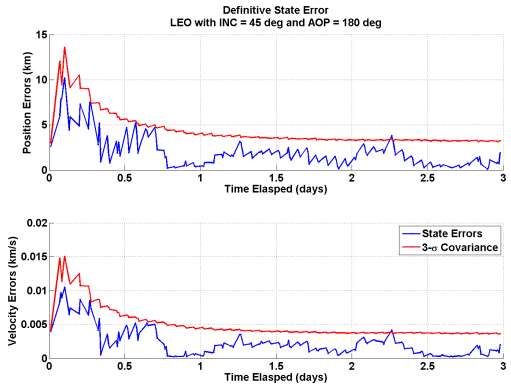

Figure 38: Definitive Error performance for a LEO with an INC of 45°, an AOP of 180°and a RAAN of 0°

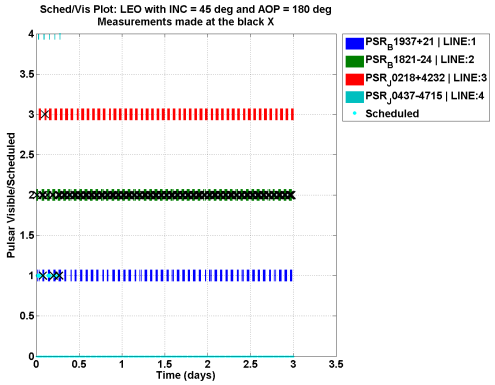

Figure 39: Pulsar Visibility/Schedule for a LEO with an INC of 45°, an AOP of 180°and a RAAN of 0°

performance. The subsequent section enumerates the discrete design range suitable for no more than 5 km position error, worst direction.

The primary indicators of XNAV performance are SMA and ECC. These orbit parameters will independently influence pulsar visibility, in-plane orbit dynamics, and the spacecraft's ambient background radiation. The two parameters determine the radial distance of the spacecraft from Earth, the value used to define both background radiation as well as occultations due to Earth. The in-plane dynamics of a spacecraft are also driven by these two parameters. The specific energy of an orbit is primarily driven by SMA, while the instantaneous velocity at a given point on an orbit is driven by ECC. The INC of an orbit also drives the environment for XNAV measurements as well as the underlying spacecraft dynamics. The occulted magnetic pole regions due to the dynamic variation of background radiation results in periodic breaks in visibility with orbits close to +/- 90°inclinations. SMA, ECC, and INC also influence the non-spherical gravitational acceleration J_2. In turn, this result modifies the rate of change of AOP and RAAN, changing the periodic timing of pulsar visibility/pulsar measurements. Finally, AOP and RAAN complete the orbit definition. Individually, they both drive the initial cadence of XNAV measure-

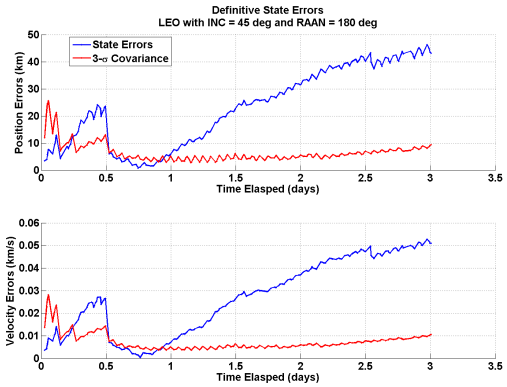

Figure 40: Definitive Error performance for a LEO with an INC of 45°, an AOP of 0°and a RAAN of 180°

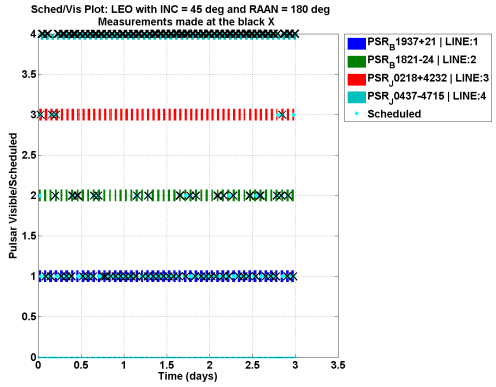

Figure 41: Pulsar Visibility/Schedule for a LEO with an INC of 45°, an AOP of 0°, and a RAAN of 180°

ments, but only minimally so.

The results here speak to individual orbital element variations. Further reasearch is required in the coupled behavior between orbit parameters in order better understand their nature.

The study is an extension of previous research by characterizing XNAV for tracking generally bounded Earth orbits. Contributions include a model of Earth background radiation as well as a novel pulsar observation scheduling algorithm. Both were created to accommodate for a general bounded Earth orbit. These models help to evaluate the application of XNAV with similar orbit regimes.

REFERENCES

[1] K.D. Anderson, D.J. Pines, and S.I. Sheikh. Validation of pulsar phase tracking for spacecraft navigation. *AIAA Journal of Guidance, Control and Dynamics*, 38 No.10:1885–1897, 2015.

[2] J.R. Carpenter and K.T. Alfriend. Navigation accuracy guidelines for orbital formation flying. *The Journal of the Astronautical Sciences*, 53 No.2:207–219, 2005.

[3] J.R. Carpenter and E.R. Schiesser. Semimajor axis knowledge and GPS orbit determination. *Navigation: Journal of the Institute of Navigation*, 48 No.1:57–68, 2001.

[4] A. Chulliat, S. Macmillian, P. Alken, C. Beggan, M. Nair, B. Hamilton, A. Woods, V. Ridley, S. Maus, and A. Thomson. The US/UK world magnetic model for 2015-2020: Technical report. *National Geophysical Data Center, NOAA*.

[5] R. T. Edwards, G. B. Hobbs, and R. N. Manchester. TEMPO2, a new pulsar timing package - II. the timing model and precision estimates. *Monthly Notices of the Royal Astronomical Society*, 372:1549–1574, November 2006.

[6] A. A. Emadzadeh and J. L. Speyer. *Navigation in space by X-ray pulsars*. Springer, 2011.

[7] ESA. ESA Space Environment Information System. `https://www.spenvis.oma.be/`, 2015.

[8] K. C. Gendreau, Z. Arzoumanian, T. Okajima, and the NICER Team. The Neutron-star Interior Composition ExploreR (NICER): an Explorer mission of opportunity for soft X-ray timing spectroscopy. In *Space Telescopes and Instrumentation: Ultraviolet to Gamma Ray*, volume 8443 of *Proc. SPIE*. International Society for Optics and Photonics, Sep 2012. doi:10.1117/12.926396.

[9] Jacob M. Hartman and Paul S. Ray. Timing accuracy for spin-powered millisecond pulsars: A comparison of predictions and rxte observations. DARPA XNAV Program Memo, 2005.

[10] John Hartnett and Andre Luiten. Colloquium: Comparison of astrophysical and terrestrial frequency standards. *Review of Modern Physics*, 83:1–9, 2011.

[11] Jason W. Mitchell, Munther A. Hassouneh, Luke M. Winternitz, Jennifer E. Valdez, Paul S. Ray, Zaven Arzoumanian, and Keith C. Gendreau. Station Explorer for X-ray Timing and Navigation Technology Architecture Overview. In *Proceedings of the 27th International Technical Meeting of the Satellite Division of the Institute of Navigation (ION GNSS+)*. Institute of Navigation, 2014.

[12] NASA. ROSAT Spacecraft Webpage. `http://science.nasa.gov/missions/rosat/`, 2015.

[13] NOAA. NOAA Geomagnetic Map. `http://www.ngdc.noaa.gov/geomag/WMM/data/WMM2015/WMM2015_F_MERC.pdf`, 2015.

[14] S. I. Sheikh. *The use of variable celestial X-ray sources for spacecraft navigation*. PhD thesis, University of Maryland, 2005.

[15] J. Van Allen and Louis Frank. Radiation around the earth to a radial distance of 107,400 km. *Nature*, 183:430–434, 1959.

[16] J. Vette. The ae-8 trapped electron model environment. *NASA Technical Report*, 1991.

[17] Luke M. B. Winternitz, Munther A. Hassouneh, Jason W. Mitchell, Fotis Gavriil, Zaven Arzoumanian, and Keith C. Gendreau. The Role of X-rays in Future Space Navigation and Communication. In *36th Annual Guidance & Navigation Control Conference*. American Astronautical Society, February 2013.

[18] Luke M. B. Winternitz, Munther A. Hassouneh, Jason W. Mitchell, Jennifer E. Valdez, Samuel R. Price, Sean R. Semper, Wayne H. Yu, Paul S. Ray, Kent S. Wood, Zaven Arzoumanian, and Keith C. Gendreau. X-ray Pulsar Navigation Algorithms and Testbed for SEXTANT. In *IEEE Aerospace Conference*. IEEE, March 2015. Accepted for publication.

[19] W. Yu. Application of x-ray pulsar navigation: A characterization of the earth orbit trade space. Master's thesis, University of Maryland, College Park, 2015.